I-8 2-92 JS (2)

PREPARED FOR THE U.S. DEPARTMENT OF ENERGY,
UNDER CONTRACT DE-AC02-76-CHO-3073

PPPL-2804
UC-427

PPPL-2804

A POST-PROCESSOR FOR THE PEST CODE

BY

S. PRIESCHE, J. MANICKAM, AND J.L. JOHNSON

January 1992

PRINCETON
PLASMA PHYSICS
LABORATORY

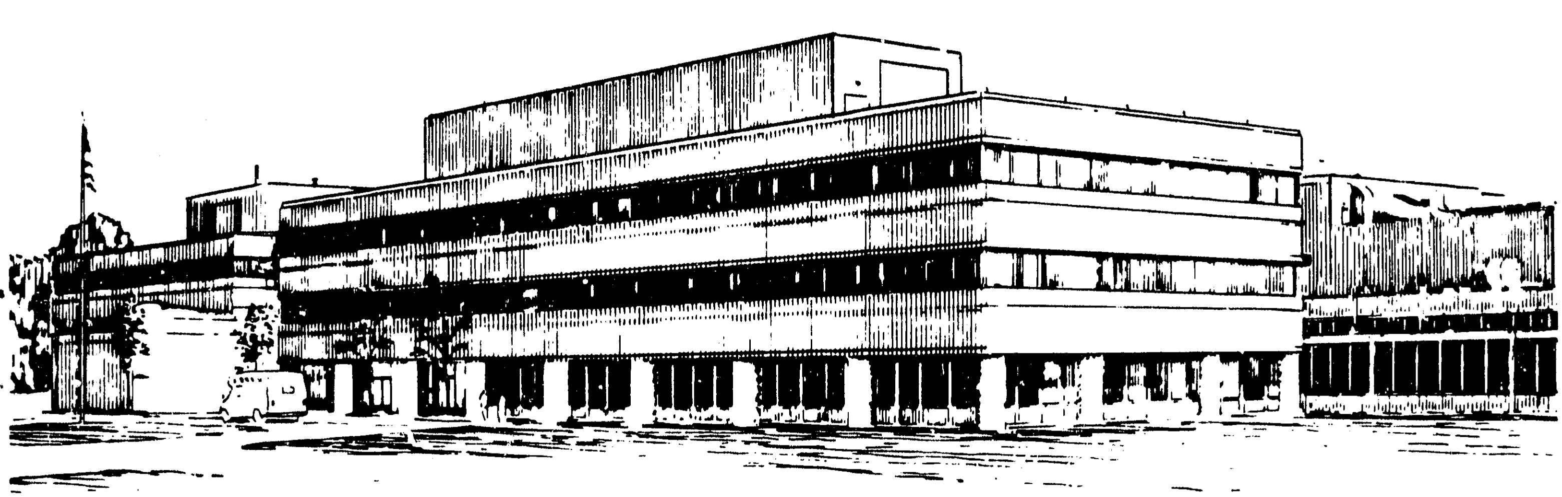

PPPL--2804

DE92 006654

A Post-Processor for the PEST Code

S. Preische, J. Manickam, and J. L. Johnson
Princeton Plasma Physics Laboratory
Princeton University

Abstract

A new post-processor has been developed for use with output from the PEST tokamak stability code. It allows us to use quantities calculated by PEST and take better advantage of the physical picture of the plasma instability which they can provide. This will improve comparison with experimentally measured quantities as well as facilitate understanding of theoretical studies.

1. Introduction

The PEST code[1] is used to determine the linear ideal MHD stability of axisymmetric tokamak configurations. It is a variational code which determines the set of displacement vectors $\boldsymbol{\xi}$ which minimizes the Lagrangian, $\delta W - \omega^2 K$, where δW and K are the potential and kinetic energies associated with perturbations from a given equilibrium. The PEST code is used for a variety of purposes including tokamak machine design, the determination of β limits and their dependence on current and pressure profiles, and study of the physics of instabilities, for example, by analysis of the mode structure. We are concentrating here on the latter use.

The mode structure of the perturbed quantities gives us some clues into the physical origin of the instability. The PEST code has not fully exploited this capability. In fact, even the usual plots of the Fourier components of ξ_ψ are misleading since they do not include the proper normalizations. To remedy this deficiency, and enhance the capabilities of the code, we have constructed a post-processor. The new code is able to:

a) construct properly normalized components of the eigenfunction $\boldsymbol{\xi}$ in order to see the true relative amplitudes of the various modes,

b) look at the eigenfunction in an orthogonal basis, as opposed to PEST's non-orthogonal basis, as an orthogonal basis may be easier to work with for some analyses,

c) compute and display quantities which can be measured experimentally, *e.g.*, components of the perturbed magnetic field $\boldsymbol{Q}$, in order to compare a known mode structure from PEST with experimental measurements, and

d) test the degree of compressibility for a specific eigenvalue by evaluating $\nabla \cdot \boldsymbol{\xi}$.

2. Formulation

2.1. *PEST representation of ξ*

For a given tokamak plasma equilibrium, with

$$\boldsymbol{B} = [f(\psi)\ \nabla\phi \times \nabla\psi \quad + \quad R\, g(\psi)\ \nabla\phi], \tag{1}$$

$$\mathcal{J} = (\nabla\psi \times \nabla\theta \cdot \nabla\phi)^{-1}, \tag{2}$$

where $\mathcal{J}$ is the Jacobian, R is the major radius of the plasma, and ψ is a normalized poloidal flux, the PEST code determines ξ_ψ^P, ξ_s^P, ξ_B^P, where the displacement vector $\boldsymbol{\xi}$ for perturbations about the equilibrium is

$$\boldsymbol{\xi} = \frac{\mathcal{J}\xi_\psi^P}{gR^2}\,\nabla\theta\times\boldsymbol{B} \;+\; \frac{i\mathcal{J}\xi_S^P}{gR^2}\,\boldsymbol{B}\times\nabla\psi \;+\; i\xi_B^P\,\boldsymbol{B}. \tag{3}$$

Each component, α, of $\boldsymbol{\xi}$ has been decomposed such that

$$\xi_\alpha^P = \sum_{m,n} \xi_{\alpha,mn}^P(\psi)e^{i(m\theta-n\phi)}. \tag{4}$$

Since axisymmetry is assumed, the Fourier coefficients for different values of n decouple and each toroidal mode number can be examined separately. However, the magnitudes of the PEST coordinates $\nabla\psi$, $\nabla\theta$, $\nabla\phi$, and the Jacobian, $\mathcal{J} = vX^2/2\pi R$ [with X the distance from the major axis to the point (ψ,θ)], have θ dependencies so that graphs of these Fourier coefficients, $\xi_{\alpha,mn}^P$, without the appropriate normalization do not descibe the physical eigenfunctions.

2.2. *Normalized components of ξ*

To get a better physical picture of the Fourier modes of the displacement vector, we define a set of unit vectors,

$$\mathbf{e}_\psi \equiv \frac{\nabla\theta\times\boldsymbol{B}}{|\nabla\theta\times\boldsymbol{B}|}, \qquad \mathbf{e}_s \equiv \frac{\boldsymbol{B}\times\nabla\psi}{B|\nabla\psi|}, \qquad \mathbf{e}_b \equiv \frac{\boldsymbol{B}}{B}, \tag{5}$$

write

$$\begin{aligned}
\boldsymbol{\xi} &= \xi_\psi\mathbf{e}_\psi + \xi_s\mathbf{e}_s + \xi_B\mathbf{e}_b \\
&= \frac{vX}{2\pi gR^3}\left[R^2g^2|\nabla\theta|^2 + f^2(\nabla\psi\cdot\nabla\theta)^2\right]^{1/2}\xi_\psi^P\,\mathbf{e}_\psi \\
&\quad + i\frac{vX|\nabla\psi|}{2\pi gR^3}\left[R^2g^2 + f^2|\nabla\psi|^2\right]^{1/2}\xi_s^P\,\mathbf{e}_s \\
&\quad + \frac{i}{X}\left[R^2g^2 + f^2|\nabla\psi|^2\right]^{1/2}\xi_B^P\,\mathbf{e}_b,
\end{aligned} \tag{6}$$

and Fourier decompose ξ_ψ, ξ_s, ξ_B in θ. This set of Fourier coefficients is properly normalized and comparision of the relative amplitudes is meaningful.

2.3. *Orthogonal projection of ξ*

Since the PEST basis vectors are not orthogonal, *i.e.*, $\nabla\psi\cdot\nabla\theta \neq 0$, it is useful to look at $\boldsymbol{\xi}$ in an orthogonal system. To do this we define a new set of orthogonal unit vectors:

$$\mathbf{e}_r \equiv \frac{\nabla\psi}{|\nabla\psi|}, \qquad \mathbf{e}_\theta \equiv \frac{\boldsymbol{B}\times\nabla\psi}{B|\nabla\psi|}, \qquad \mathbf{e}_b \equiv \frac{\boldsymbol{B}}{B}. \tag{7}$$

Then we can write:

$$\begin{aligned} \boldsymbol{\xi} &= \xi_r \mathbf{e}_r + \xi_\theta \mathbf{e}_\theta + \xi_B \mathbf{e}_b \\ &= \frac{\xi_\psi^P}{R|\nabla\psi|}\,\mathbf{e}_r \\ &+ \frac{vX|\nabla\psi|}{2\pi g R^3}\left[R^2g^2 + f^2|\nabla\psi|^2\right]^{1/2}\left(i\xi_s^P - \frac{(\nabla\psi\cdot\nabla\theta)\xi_\psi^P}{|\nabla\psi|^2}\right)\mathbf{e}_\theta \\ &+ \frac{i}{X}\left[R^2g^2 + f^2|\nabla\psi|^2\right]^{1/2}\xi_B^P\,\mathbf{e}_b. \end{aligned} \tag{8}$$

This form is useful for looking at radial displacements, as $\mathbf{e}_r$ is always perpendicular to a flux surface and in a toroidal cross section, whereas $\mathbf{e}_\psi$ has components in all three coordinate directions, because

$$\nabla\theta\times\boldsymbol{B} = \frac{Rg\mathcal{J}|\nabla\theta|^2}{X^2}\,\nabla\psi - \frac{Rg\mathcal{J}(\nabla\psi\cdot\nabla\theta)}{X^2}\,\nabla\theta + f(\nabla\psi\cdot\nabla\theta)\,\nabla\phi. \tag{9}$$

Note, however, that $\mathbf{e}_\theta$ does not lie completely in a toroidal cross section.

2.4. *Perturbed magnetic field*

Another interesting quantity is the perturbed magnetic field, $\boldsymbol{Q} = \nabla\times(\boldsymbol{\xi}\times\boldsymbol{B})$, which can be measured with Mirnov loops.

$$\begin{aligned} \boldsymbol{Q} = &\left[\frac{\mathcal{J}f}{X^2gR}(\nabla\psi\cdot\nabla\theta)\frac{\partial g}{\partial\psi}\xi_\psi^P + \frac{\mathcal{J}g}{X^2R}(\nabla\psi\cdot\nabla\theta)\frac{\partial}{\partial\psi}\left(\frac{f\xi_\psi^P}{g}\right) + \frac{\mathcal{J}f}{X^2R}|\nabla\theta|^2\frac{\partial\xi_\psi^P}{\partial\theta}\right. \\ &\left. + \frac{f^2}{X^2gR}\frac{\partial\xi_\psi^P}{\partial\phi} + \frac{\mathcal{J}^2B^2}{X^2gR^2}\left(|\nabla\theta|^2\frac{\partial\xi_\psi^P}{\partial\phi} - i\,\nabla\psi\cdot\nabla\theta\,\frac{\partial\xi_s^P}{\partial\phi}\right)\right]\nabla\psi \\ &- \left[\frac{\mathcal{J}f}{X^2gR}|\nabla\psi|^2\frac{\partial g}{\partial\psi}\xi_\psi^P + \frac{\mathcal{J}g}{X^2R}|\nabla\psi|^2\frac{\partial}{\partial\psi}\left(\frac{f\xi_\psi^P}{g}\right)\right. \\ &\left. + \frac{\mathcal{J}f}{X^2R}(\nabla\psi\cdot\nabla\theta)\frac{\partial\xi_\psi^P}{\partial\theta} + \frac{\mathcal{J}^2B^2}{X^2gR^2}\left(\nabla\psi\cdot\nabla\theta\frac{\partial\xi_\psi^P}{\partial\phi} - i|\nabla\psi|^2\,\frac{\partial\xi_s^P}{\partial\phi}\right)\right]\nabla\theta \end{aligned} \tag{10}$$

$$
+\left[\frac{f\xi_\psi^P}{gR^2}\left\{\frac{\partial}{\partial\psi}\left(\frac{f\mathcal{J}}{X^2}|\nabla\psi|^2\right)+\frac{\partial}{\partial\theta}\left(\frac{f\mathcal{J}}{X^2}\nabla\psi\cdot\nabla\theta\right)\right\}+\frac{f}{R^2}|\nabla\psi|^2\frac{\partial}{\partial\psi}\left(\frac{f\xi_\psi^P}{g}\right)\right.
$$
$$
\left.-\frac{X^2}{\mathcal{J}R^2}\left\{\frac{\partial}{\partial\psi}\left(\frac{\mathcal{J}B^2\xi_\psi^P}{g}\right)+i\frac{\partial}{\partial\theta}\left(\frac{\mathcal{J}B^2\xi_s^P}{g}\right)\right\}+\frac{f^2}{gR^2}(\nabla\psi\cdot\nabla\theta)\frac{\partial\xi_\psi^P}{\partial\theta}\right]\nabla\phi.
$$

The most useful components of $\boldsymbol{Q}$ for experimental measurements are

$$
Q_\psi=\frac{\boldsymbol{Q}\cdot\nabla\psi}{|\nabla\psi|},\qquad Q_\theta=\frac{\boldsymbol{Q}\cdot(\nabla\phi\times\nabla\psi)}{|\nabla\phi||\nabla\psi|},\qquad Q_\phi=\frac{\boldsymbol{Q}\cdot\nabla\phi}{|\nabla\phi|},\tag{11}
$$

where the component Q_θ now lies in a toriodal cross section. These components are

$$
Q_\psi=\frac{1}{X^2|\nabla\psi|}\left\{\frac{2\pi f}{\upsilon}\frac{\partial\xi_\psi^P}{\partial\theta}+g\frac{\partial\xi_\psi^P}{\partial\phi}\right\},\tag{12}
$$

$$
\begin{aligned}
Q_\theta \;=\;& -\frac{|\nabla\psi|}{XR}\left[f\frac{\partial\xi_\psi^P}{\partial\psi}+\xi_\psi^P\frac{\partial f}{\partial\psi}\right]-\frac{f}{XR|\nabla\psi|}(\nabla\psi\cdot\nabla\theta)\frac{\partial\xi_\psi^P}{\partial\theta}\\
&-\frac{\upsilon^2}{4\pi^2 gR^3}\left[f^2|\nabla\psi|^2+R^2g^2\right]\left[(\nabla\psi\cdot\nabla\theta)\frac{\partial\xi_\psi^P}{\partial\phi}-i|\nabla\psi|^2\frac{\partial\xi_s^P}{\partial\phi}\right],
\end{aligned}\tag{13}
$$

$$
\begin{aligned}
Q_\phi \;=\;& +\frac{fX^2\xi_\psi^P}{gR^2}\left\{\frac{\partial}{\partial\psi}\left(\frac{f\mathcal{J}}{X^2}|\nabla\psi|^2\right)+\frac{\partial}{\partial\theta}\left(\frac{f\mathcal{J}}{X^2}\nabla\psi\cdot\nabla\theta\right)\right\}\\
&+\frac{fX^2}{R^2}|\nabla\psi|^2\frac{\partial}{\partial\psi}\left(\frac{f\xi_\psi^P}{g}\right)+\frac{f^2X^2}{gR^2}(\nabla\psi\cdot\nabla\theta)\frac{\partial\xi_\psi^P}{\partial\theta}\\
&-\frac{X^4}{\mathcal{J}R^2}\left\{\frac{\partial}{\partial\psi}\left(\frac{\mathcal{J}B^2\xi_\psi^P}{g}\right)+i\frac{\partial}{\partial\theta}\left(\frac{\mathcal{J}B^2\xi_s^P}{g}\right)\right\}.
\end{aligned}\tag{14}
$$

2.5. *Evaluation of compressibility*

The post-processor can also be used to determine how well the incompressibility assumption, $\nabla\cdot\boldsymbol{\xi}=0$, is satisfied. This is done by calculating

$$
\begin{aligned}
\nabla\cdot\boldsymbol{\xi} \;=\;& \frac{1}{X^2R}\frac{\partial(X^2\xi_\psi^P)}{\partial\psi}+\frac{i}{X^2R}\frac{\partial(X^2\xi_s^P)}{\partial\theta}\\
&+\frac{\upsilon f}{2\pi gR^3}\left[\nabla\psi\cdot\nabla\theta\frac{\partial\xi_\psi^P}{\partial\phi}-i|\nabla\psi|^2\frac{\partial\xi_s^P}{\partial\phi}\right]\\
&+\frac{i2\pi Rf}{\upsilon X^2}\frac{\partial\xi_B^P}{\partial\theta}+\frac{iRg}{X^2}\frac{\partial\xi_B^P}{\partial\phi}.
\end{aligned}\tag{15}
$$

3. Applications

We now demonstrate some applications of computing these quantities from the PEST output.

The new Fourier decomposition of the different projections of the displacement vector give a better physical picture for analysis of the instability's mode structure.

$\boldsymbol{Q}$ can be calculated at any point inside the plasma and compared with experimentally measured values. The components of $\boldsymbol{Q}$, may also be Fourier decomposed to look at the mode structure. As an example of more direct comparision with experiments, the signal $\partial\tilde{B}/\partial t$ from a poloidal array of Mirnov coils can be Fourier decomposed in θ to find the amplitudes of the various poloidal modes. These measurements of the perturbed field can then be compared with $Q_{\alpha,mn}(\psi)$ by noting that the mth component of the field decays as $r^{-(m+1)}$.

$$Q_{\alpha,mn}(r,\theta,\phi) = Q_{\alpha,mn}(a,0,0)\left(\frac{a}{r}\right)^{m+1}\cos(m\theta+n\phi), \tag{16}$$

where a is the plasma minor radius.

The importance of the compressible term in δW can be measured by comparing the $\gamma p|\boldsymbol{\nabla}\cdot\boldsymbol{\xi}|^2$ term with the other terms in δW,

$$\begin{aligned}\delta W = \frac{1}{2}\int_{plasma} dV\Bigg[&\frac{|\boldsymbol{Q}_\perp|^2}{\mu_o}+\frac{B^2}{\mu_o}|\boldsymbol{\nabla}\cdot\boldsymbol{\xi}_\perp+2\boldsymbol{\xi}_\perp\cdot\boldsymbol{\kappa}|^2 \\ &-2\,(\boldsymbol{\xi}_\perp\cdot\boldsymbol{\nabla}p)(\boldsymbol{\xi}_\perp^*\cdot\boldsymbol{\kappa})-J_\parallel(\boldsymbol{\xi}_\perp^*\times\hat{\boldsymbol{b}})\cdot\boldsymbol{Q}_\perp \\ &+\gamma p|\boldsymbol{\nabla}\cdot\boldsymbol{\xi}|^2\Bigg].\end{aligned} \tag{17}$$

3.1. *Pressure modified kink mode*

We first consider a large aspect ratio ($R/a = 10$) circular cross-section discharge, which is chosen to illustrate pressure modification of an external kink mode. The parameters defining this case are: $\beta = 0.69\%$, $\beta_p = 4.97$, $q(0) = 1.05$, $q(1) = 2.95$, Troyon factor $C_T \equiv \beta aB/I = 3.69$. This configuration is unstable with respect to the global instability shown in Fig. 1 with an eigenvalue $\rho a^2\omega^2/\mu_0 B^2 = 0.247$. The Fourier decomposition of the displacement that is presently available from the PEST code, ξ_ψ^P of Eq. (3), is shown in Fig. 2. The decomposition of the properly normalized component, ξ_ψ of Eq. (6), is shown in Fig. 3. The decomposition in the orthogonal projection, ξ_r of Eq. (8), is very similar in both magnitude and form to Fig. 3. The change in normalization between ξ_ψ^P and ξ_ψ modifies the relative magnitudes and introduces sign changes in the modes as well as an $m = 0$ component. This indicates that the lower-m modes contribute much more to the instability than one would have believed from looking at the original decomposition. The behavior of the displacement ξ_θ of Eq. (8) is given in Fig. 4. It has some of the properties of ξ_ψ and ξ_r, but is far from identical. We do not show the component ξ_b, which represents the flow along the field line that is necessary to minimize $\nabla \cdot \boldsymbol{\xi}$, since it is small. The quantity $\nabla \cdot \boldsymbol{\xi}$ on several flux surfaces is illustrated in Fig. 5. The components of the perturbed field, Q_ψ and Q_θ, that are associated with this displacement are shown in Figs. 6 and 7. The Fourier decompositions of Q_ψ and Q_θ are shown in Figs. 8 and 9. Comparison of these with ξ_ψ in Fig. 3 shows somewhat different structures.

3.2. *External kink mode*

Our second illustration is also a large aspect ratio circular cross-section plasma. It is unstable with respect to an $m = 3$ current driven kink mode. The discharge has $\beta = 0$, $q(0) = 1.05$ and $q(1) = 2.95$. The fastest growing instability, with $\rho a^2\omega^2/\mu_0 B^2 = 0.004$, is localized near the plasma surface as can be seen in Fig. 10. The perturbed field on a flux surface, Fig. 11, shows a nearly pure $m = 3$ mode that is localized near the edge. Nevertheless, plots of a Fourier decomposition of the perturbed magnetic field in Figs. 12 and 13 show coupling to neighboring harmonics.

3.3. *Ballooning mode*

Our third case is a low aspect ratio ($R/a = 3.33$), elliptic cross-section discharge chosen to illustrate a high-n ballooning mode instability. The plasma boundary is defined by

$$X = R + a\cos(\theta + \delta \sin\theta), \tag{18}$$

$$Z = a\sin(\theta + \delta\sin\theta), \tag{19}$$

with $\kappa = 1.5$ and $\delta = 0.26$. We have $\beta = 6.33\%$, $\beta_p = 2.62$, $q(0) = 1.15$, $q(1) = 4.54$, and $C_T = 6.92$. The dominant instability, Fig. 14, has a large growth rate, $\rho a^2\omega^2/\mu_0 B^2 = 1.10$, and has a strong ballooning character. The Fourier decompositions of the displacement vectors normal to the magnetic field, ξ_r and ξ_θ, are given in Figs. 15 and 16, and $\nabla \cdot \boldsymbol{\xi}$ is given in Fig. 17. These, together with pictures of the perturbed magnetic field, such as Figs. 18 and 19, show that this ballooning mode contains much more structure than might have been anticipated.

An application of this processor is to compare the contributions from the various terms in δW, Eq. (17). For example, the comparison of the $|\boldsymbol{Q}_\perp|^2/\mu_o$ term with $\gamma p|\nabla \cdot \boldsymbol{\xi}|^2$ on a surface in Fig. 20 shows that the sloshing of sound waves to equilize the pressure on the magnetic surfaces can be roughly 5% of the stabilization effect associated with shear Alfvén waves.

4. Summary

We can now calculate many quantities of physical interest using given tokamak equilibrium values and the eigenfunctions $\boldsymbol{\xi}$ found by the PEST code. Application of this program has already proven to be useful in analysis of data from PBX-M plasmas[2] .

As an extension of this work, values of the perturbed field, $\boldsymbol{Q}$, can be predicted for a given instability at any point outside the plasma by using the extrapolation of Eq. (16). This will provide direct comparison with experimental measurements.

At present, we calculate and plot only some of the terms in δW. Calculating all of these terms will provide an opportunity to investigate the sources of energy drive and stabilization for a particular unstable mode, shedding light on mechanisms for optimizing the stability properties of a configuration.

5. Acknowledgment

This work was supported by the U. S. Department of Energy contract No. DE-AC02-76-CHO-3073 with Princeton University. Much of the work was performed while one of us (SP) was under appointment to the Magnetic Fusion Science Fellowship program, U. S. Department of Energy.

References

1. R. C. Grimm, J. M. Greene, and J. L. Johnson, in *Methods in Computational Physics.* Edited by J. Killeen (Academic Press, New York, 1976) Vol. 16, p. 253.

2. D. W. Roberts, Ph. D. Thesis, Princeton University, 1991.

Figures

Fig. 1. Displacement vector for the pressure modified kink mode. The length denotes the magnitude of the displacement at a point located at the start of the arrow.

Fig. 2. Fourier decomposition of the unnormalized perturbation, ξ_ψ^P, for the pressure modified kink mode.

Fig. 3. Fourier decomposition of the normalized perturbation, ξ_ψ, for the pressure modified kink mode.

Fig. 4. Fourier decomposition of ξ_θ, the normalized orthogonal perturbation in the $\boldsymbol{B} \times \boldsymbol{\nabla}\psi$ direction, for the pressure modified kink mode.

Fig. 5. The function $\boldsymbol{\nabla} \cdot \boldsymbol{\xi}$ for the pressure modified kink mode as a function of θ on a magnetic surface.

Fig. 6. Contour plot of Q_ψ for the pressure modified kink mode. The solid lines denote fields in the positive Q_ψ direction; the dotted lines are for fields in the opposite direction.

Fig. 7. Contour plot of Q_θ for the pressure modified kink mode.

Fig. 8. Fourier decomposition of the perturbed field, Q_ψ, perpendicular to a flux surface for the pressure modified kink mode.

Fig. 9. Fourier decomposition of the component of the perturbed field, Q_θ, for the pressure modified kink mode.

Fig. 10. Displacement vector for the external kink mode.

Fig. 11. The perturbed field Q_θ as a function of θ for the external kink mode.

Fig. 12. Fourier decomposition of the perturbed field Q_ψ for the external kink mode.

Fig. 13. Fourier decomposition of the perturbed magnetic field Q_θ for the external kink mode.

Fig. 14. Displacement vector for the ballooning mode.

Fig. 15. Fourier decomposition of the normalized orthogonal radial perturbation, ξ_r, for the ballooning mode.

Fig. 16. Fourier decomposition of the normalized orthogonal perturbation ξ_θ for the ballooning mode.

Fig. 17. The function $\nabla \cdot \boldsymbol{\xi}$ for the ballooning mode as a function of θ on a magnetic surface.

Fig. 18. Contour plot of Q_ψ for the ballooning mode.

Fig. 19. Q_θ as a function of θ for the ballooning mode.

Fig. 20. The $|\boldsymbol{Q}_\perp|^2/\mu_o$ and $\gamma p|\nabla \cdot \boldsymbol{\xi}|^2$ terms in δW on a surface with $\psi = 0.1$ for the ballooning mode.

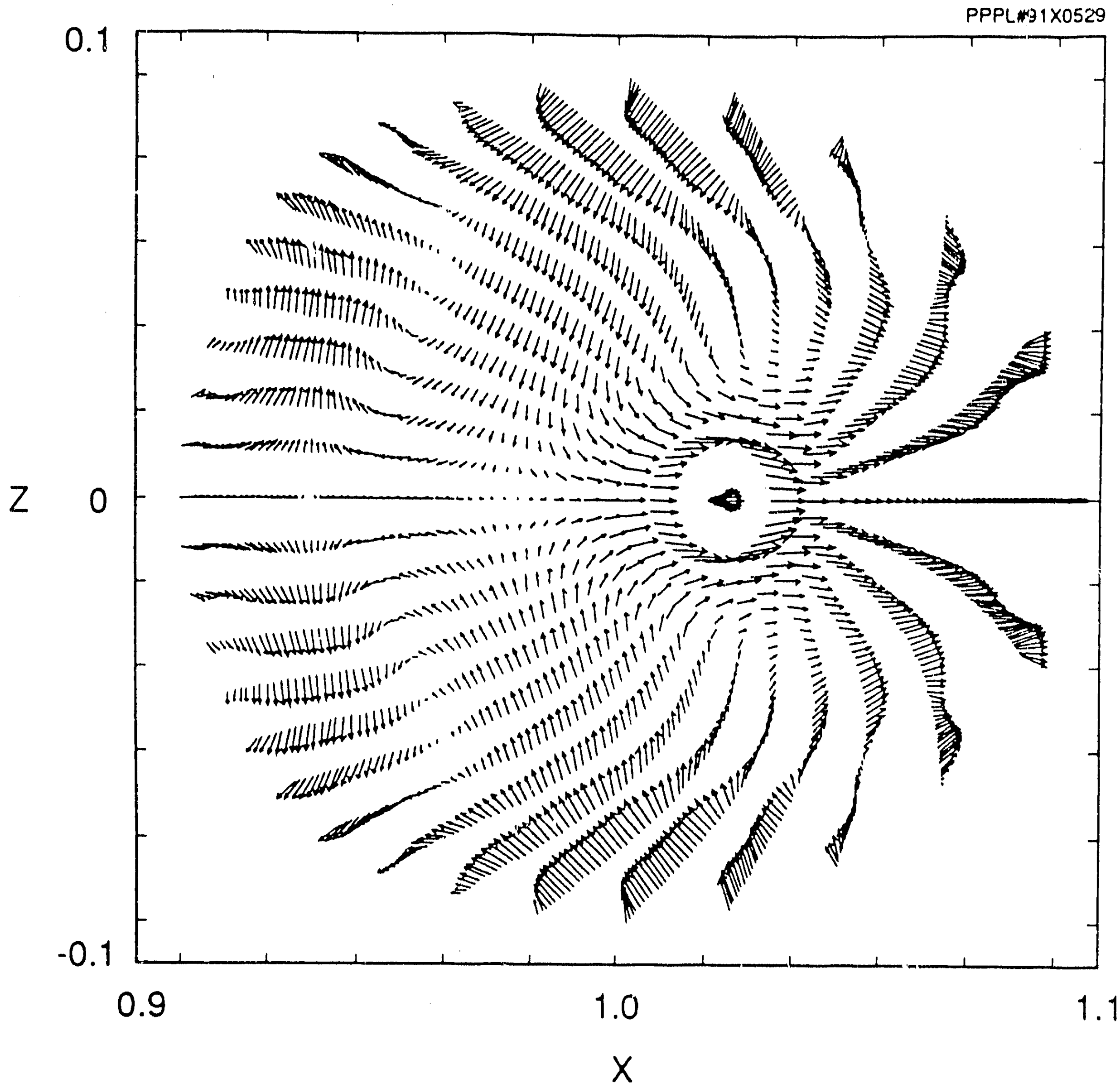

Fig. 1

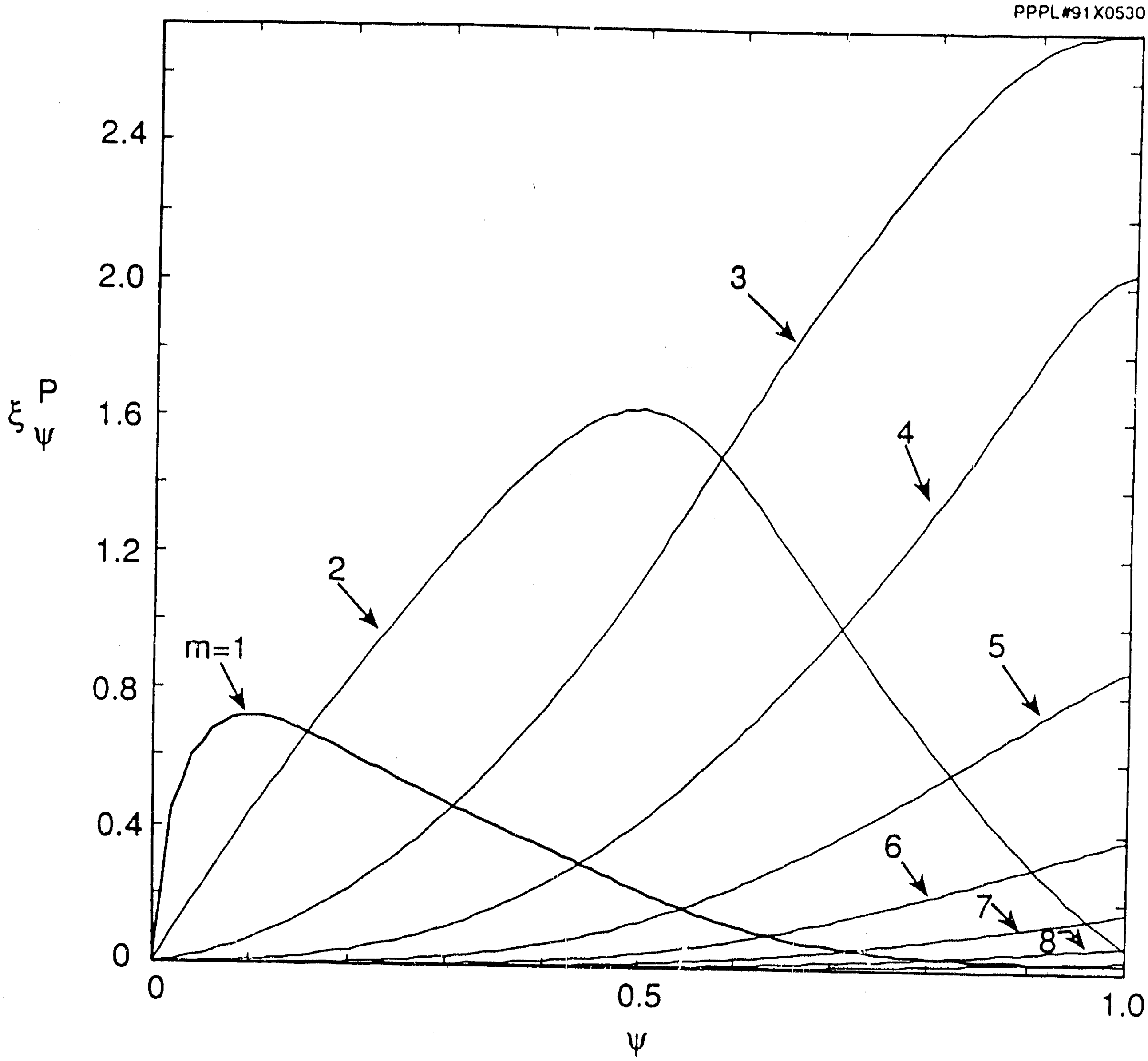

Fig. 2

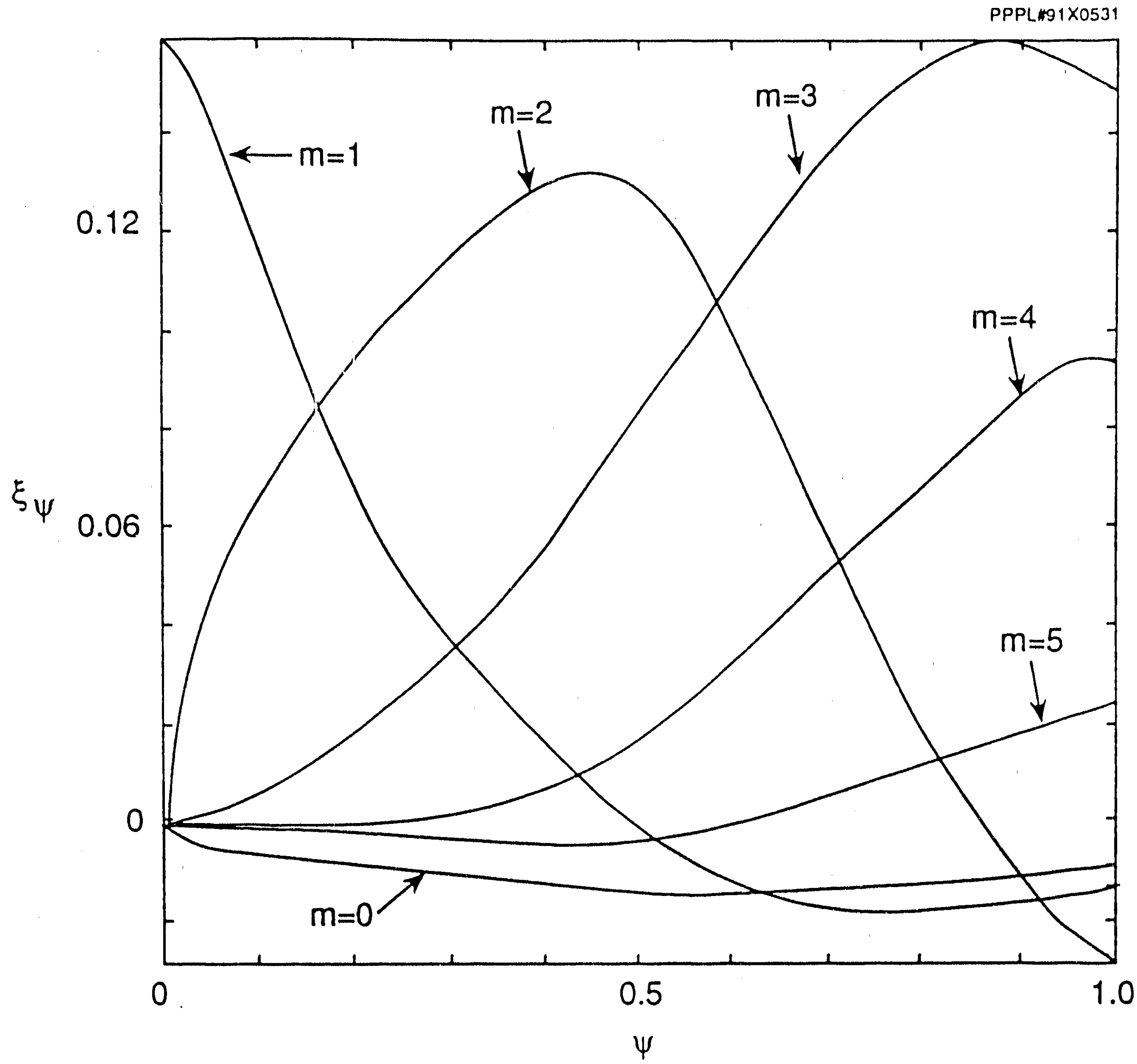

Fig. 3

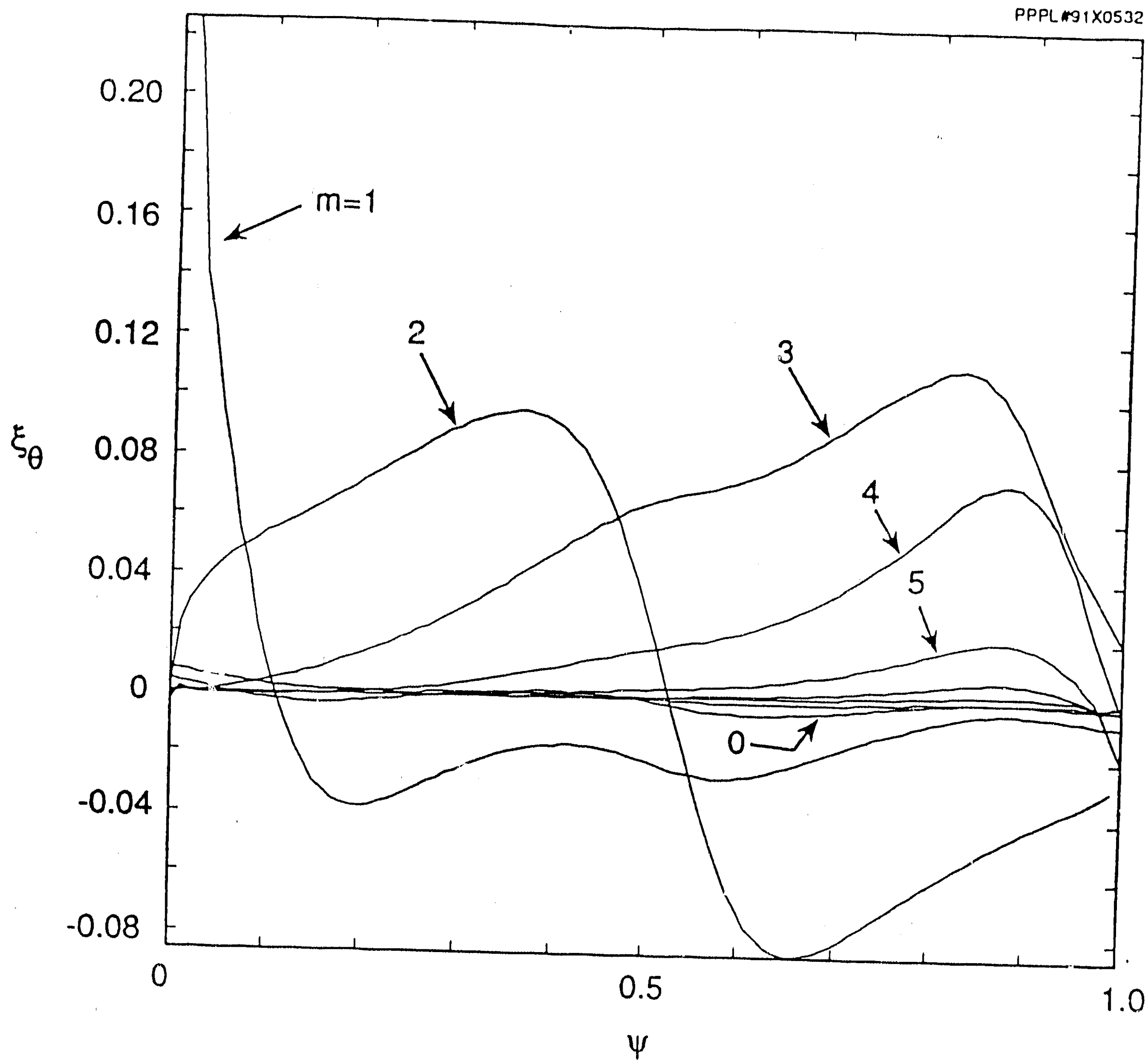

PPPL#91X0532
0.20
0.16
0.12
0.08
0.04
0
-0.04
-0.08
ξ_θ
m=1
2
3
4
5
0
0
0.5
1.0
ψ

Fig. 4

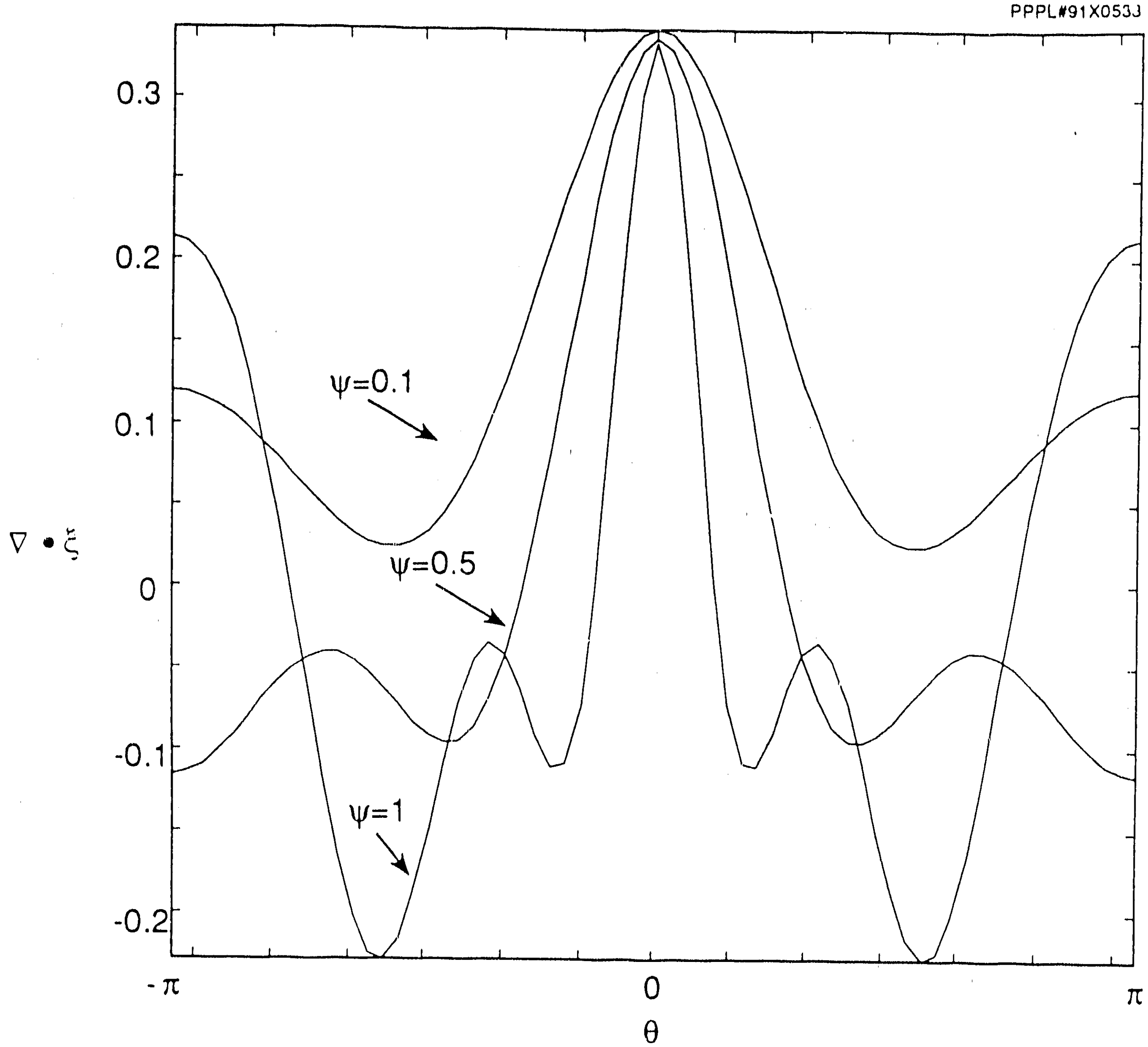

Fig. 5

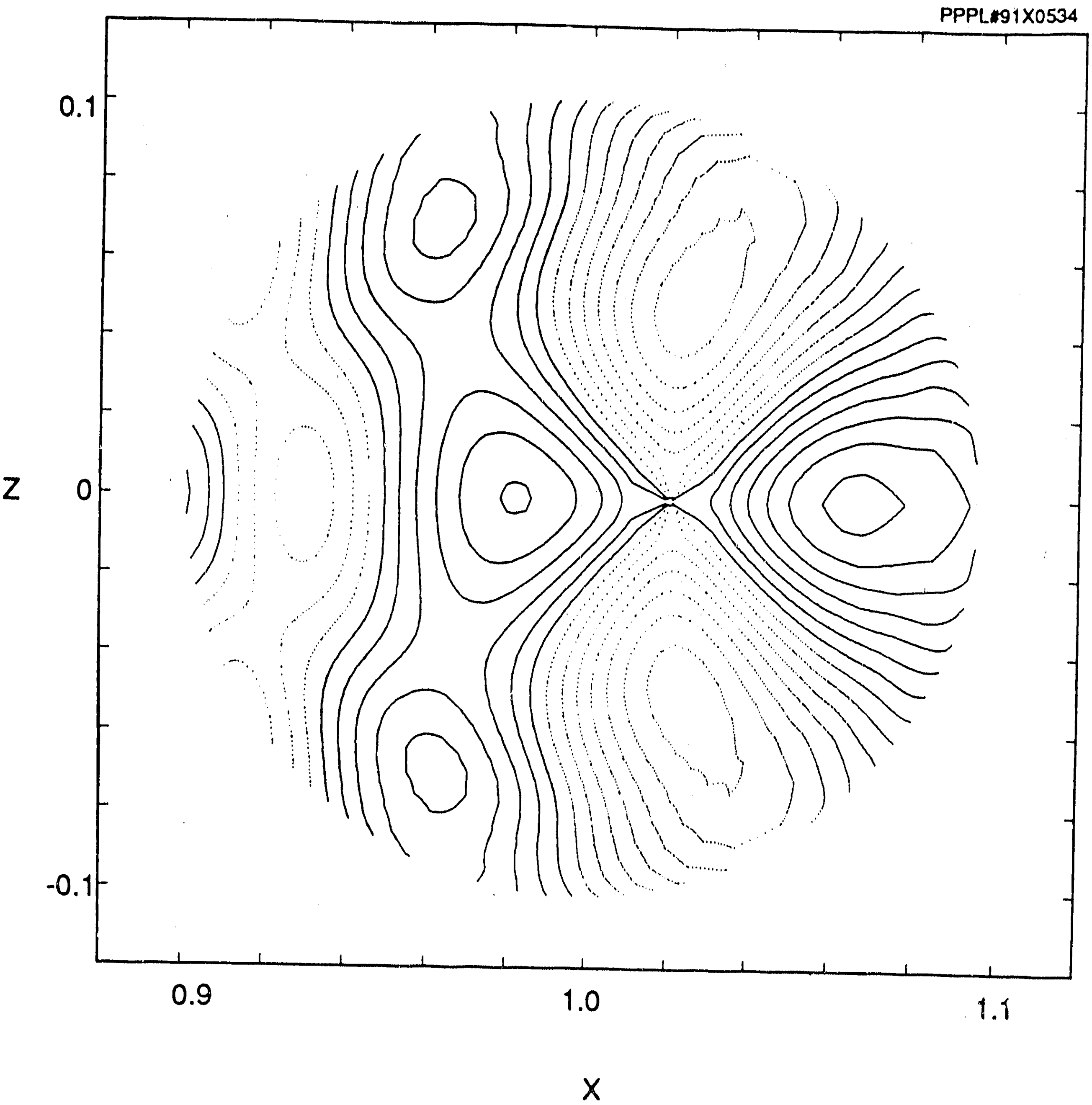

Fig. 6

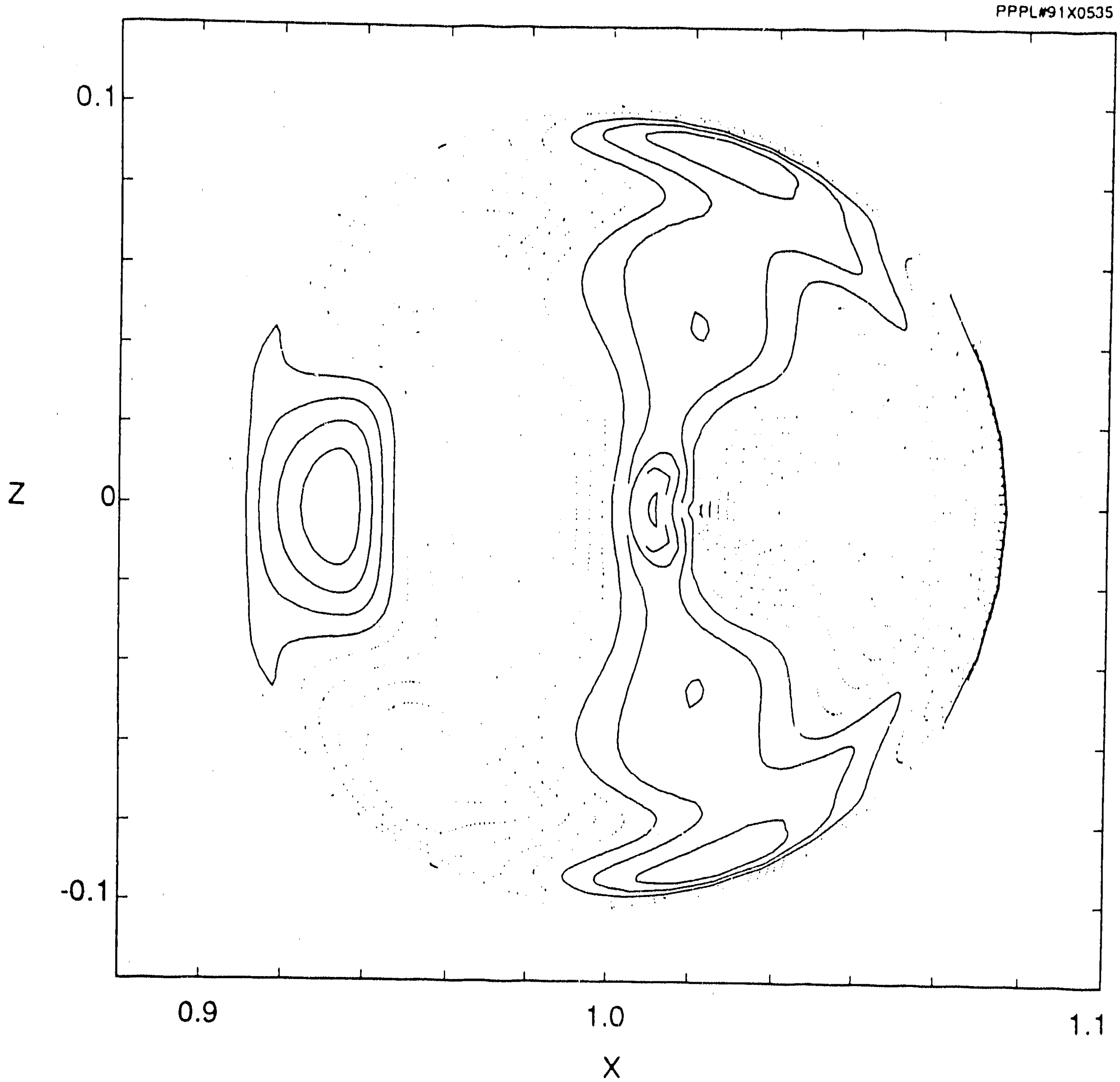

Fig. 7

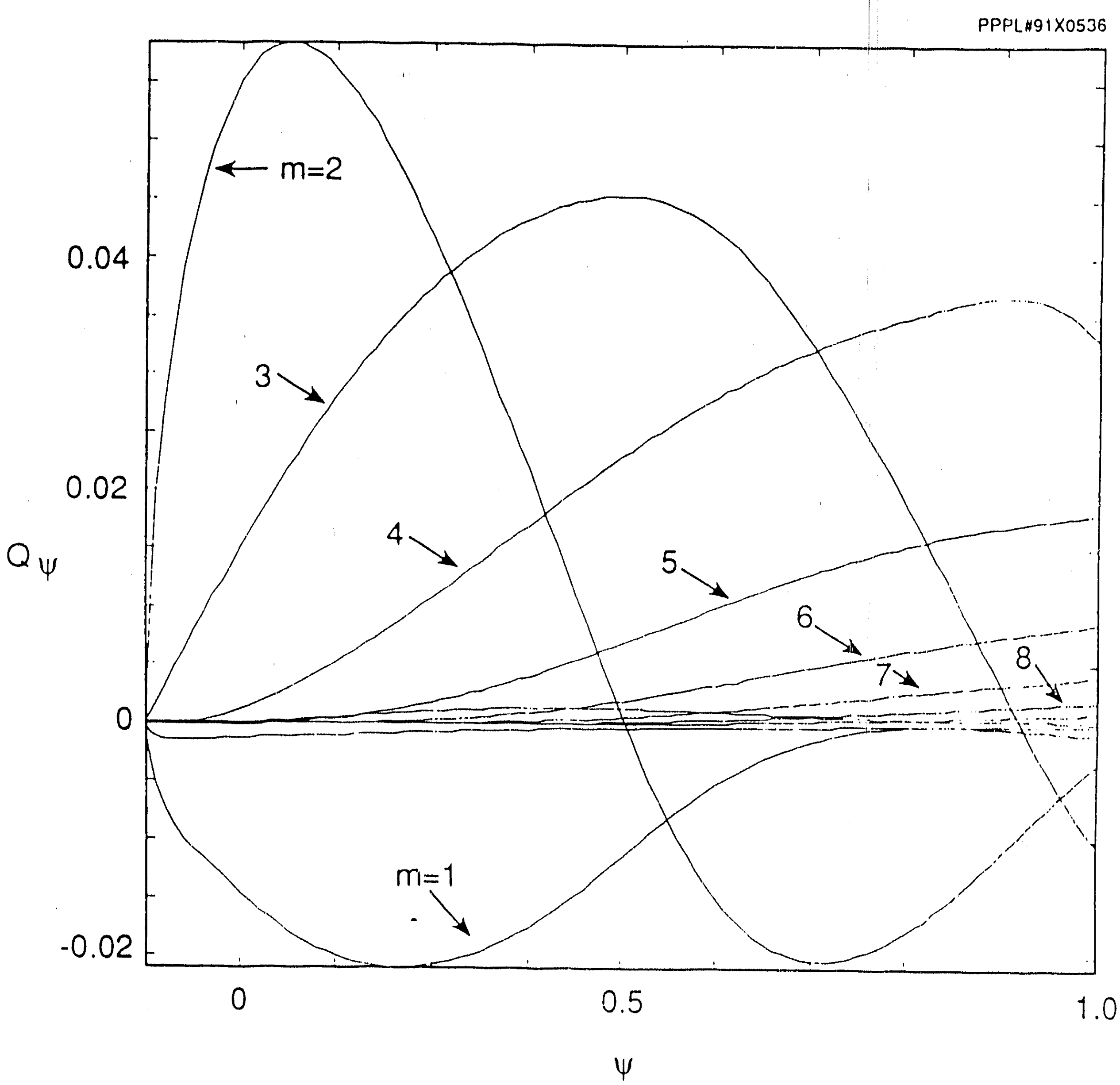

Fig. 8

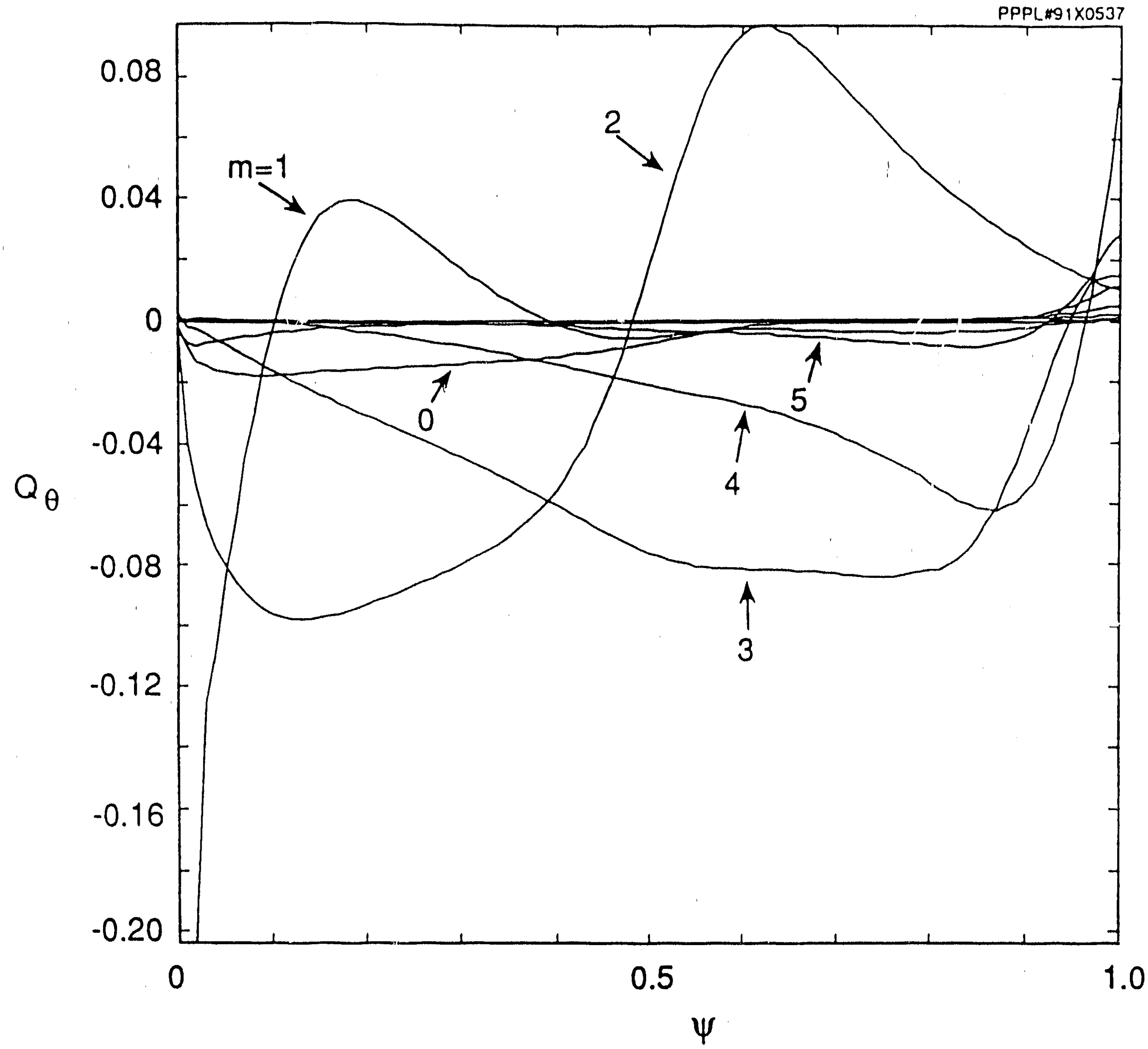
PPPL#91X0537
0.08
0.04
0
-0.04
-0.08
-0.12
-0.16
-0.20
Q_θ
0
0.5
1.0
ψ
m=1
2
0
5
4
3

Fig. 9

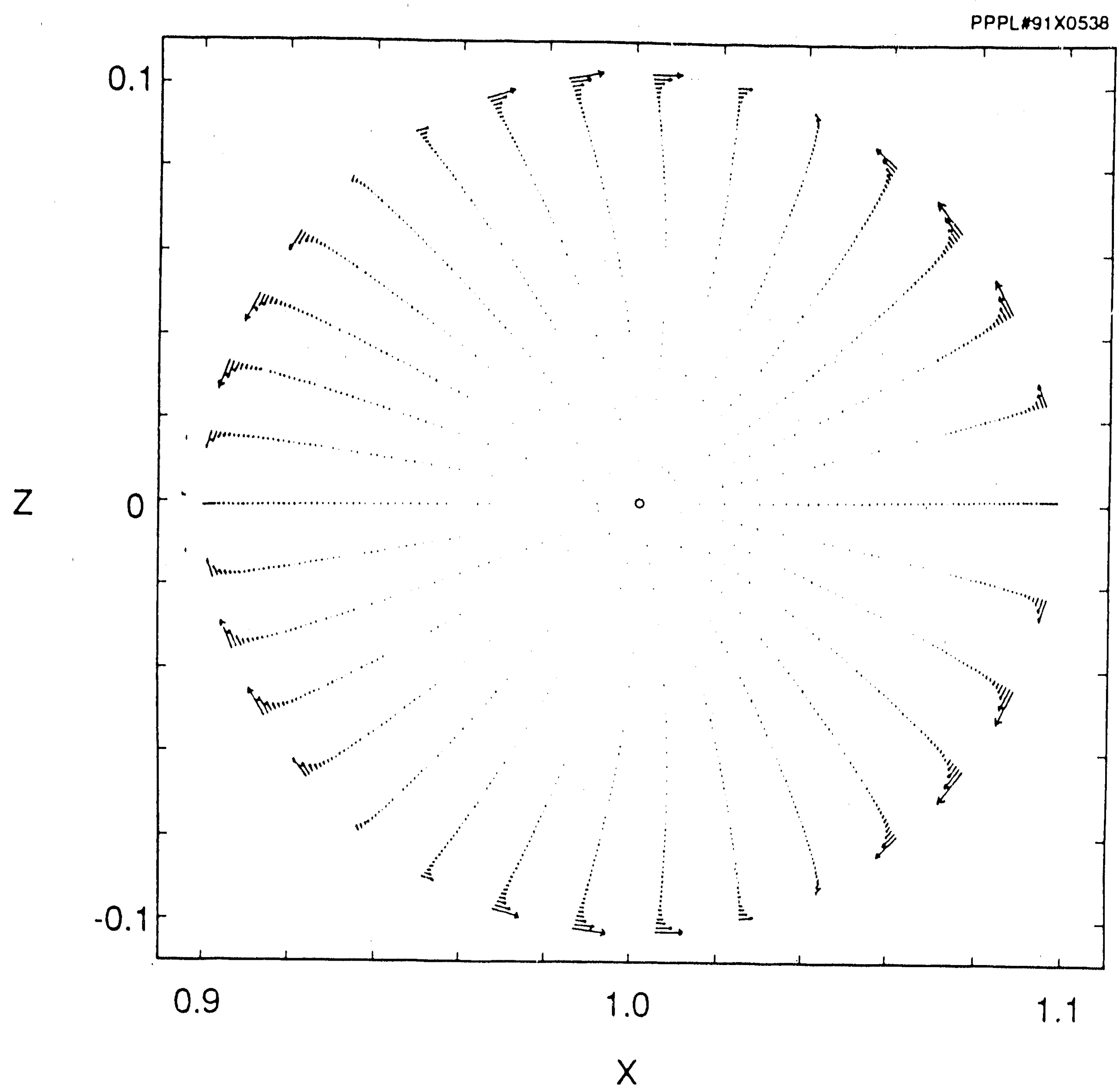

Fig. 10

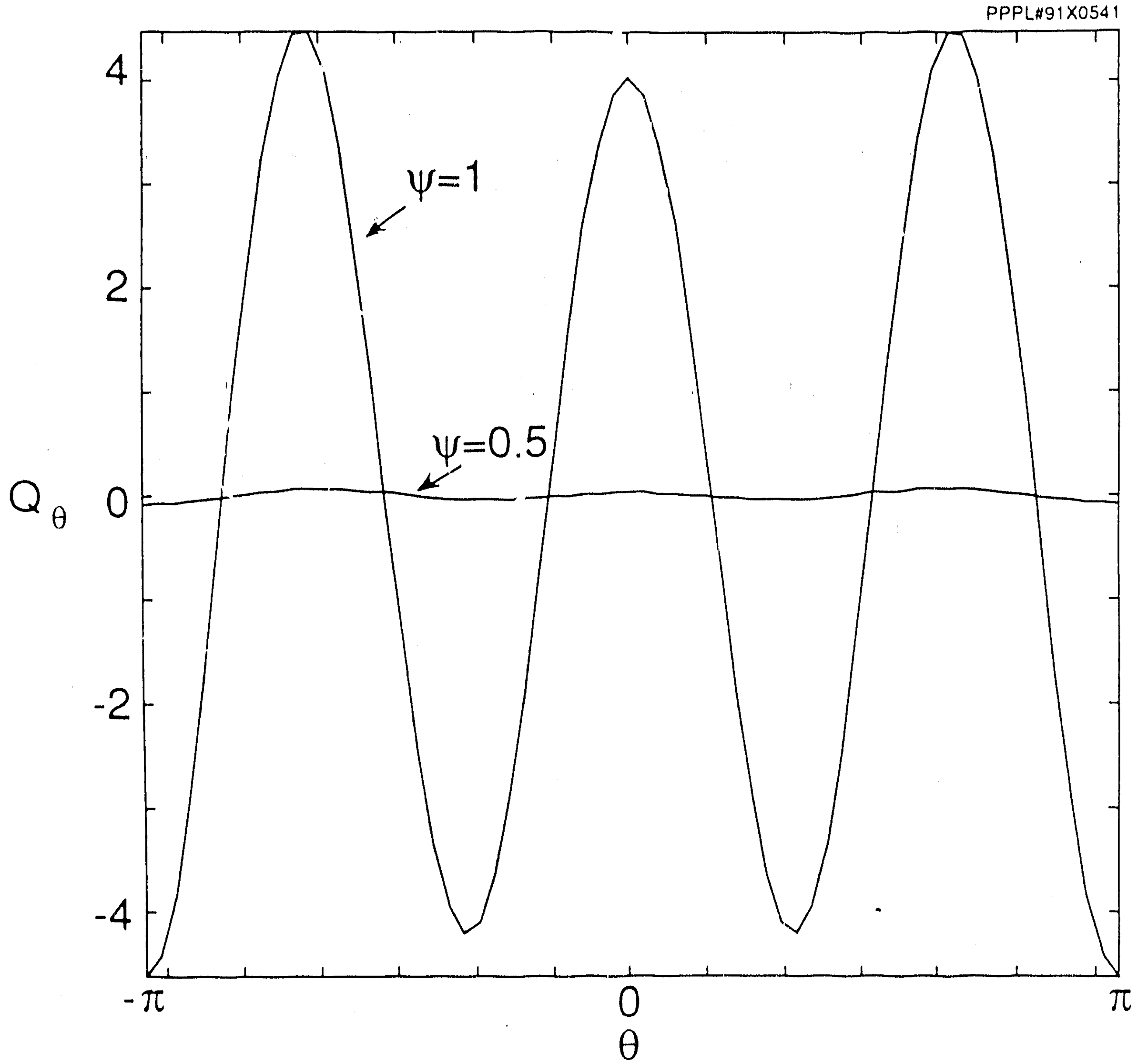

Fig. 11

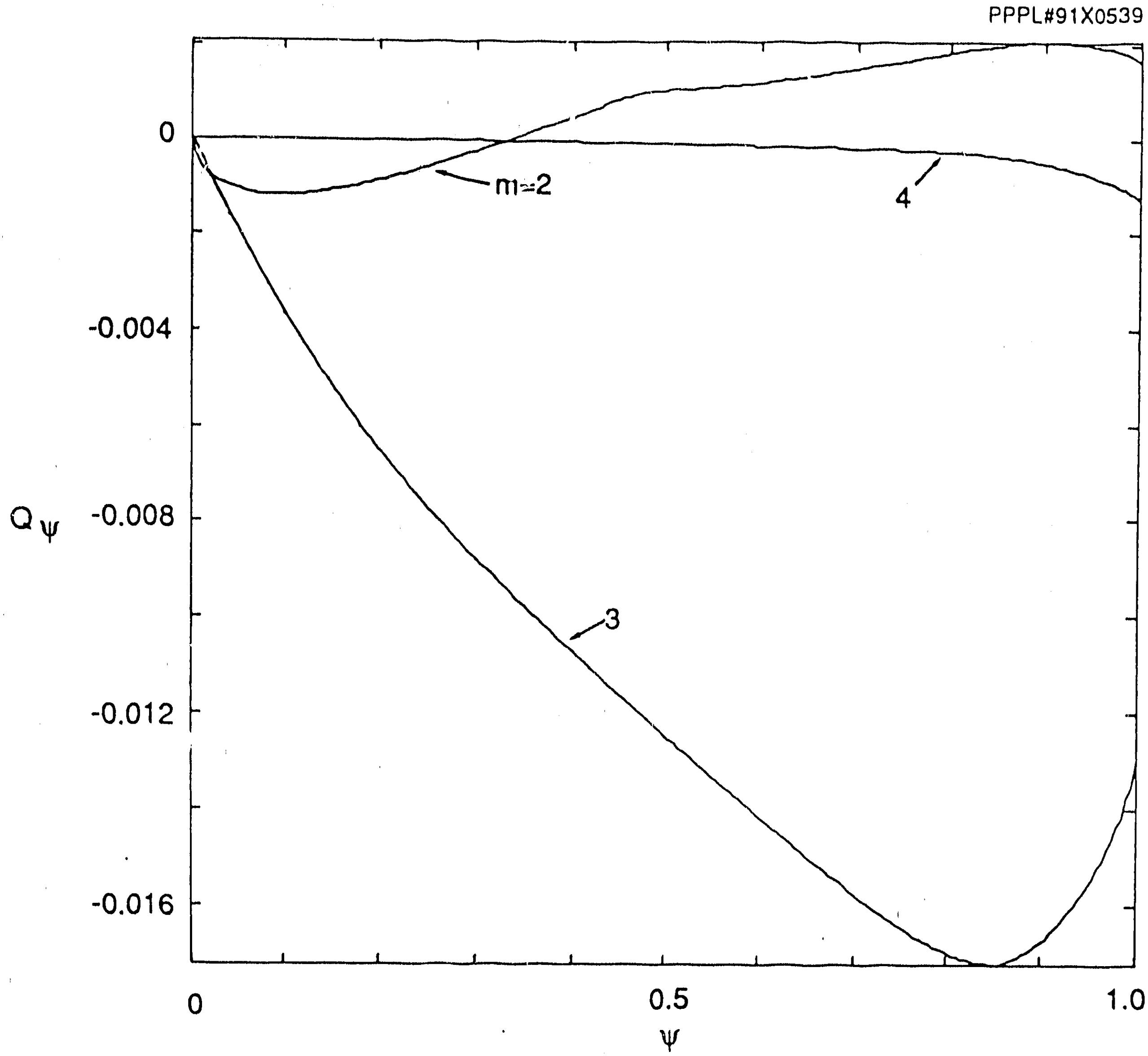

Fig. 12

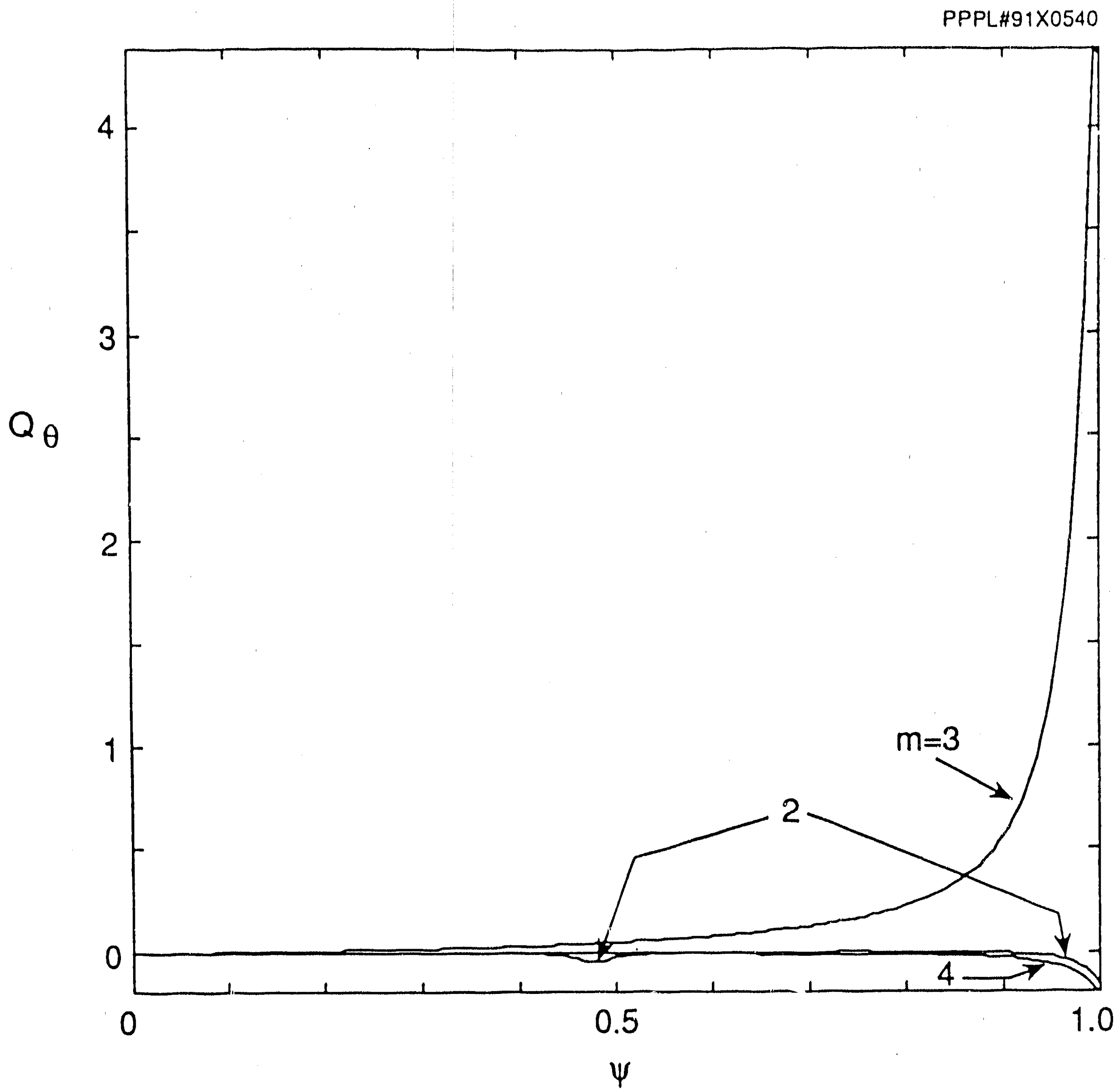

Fig. 13

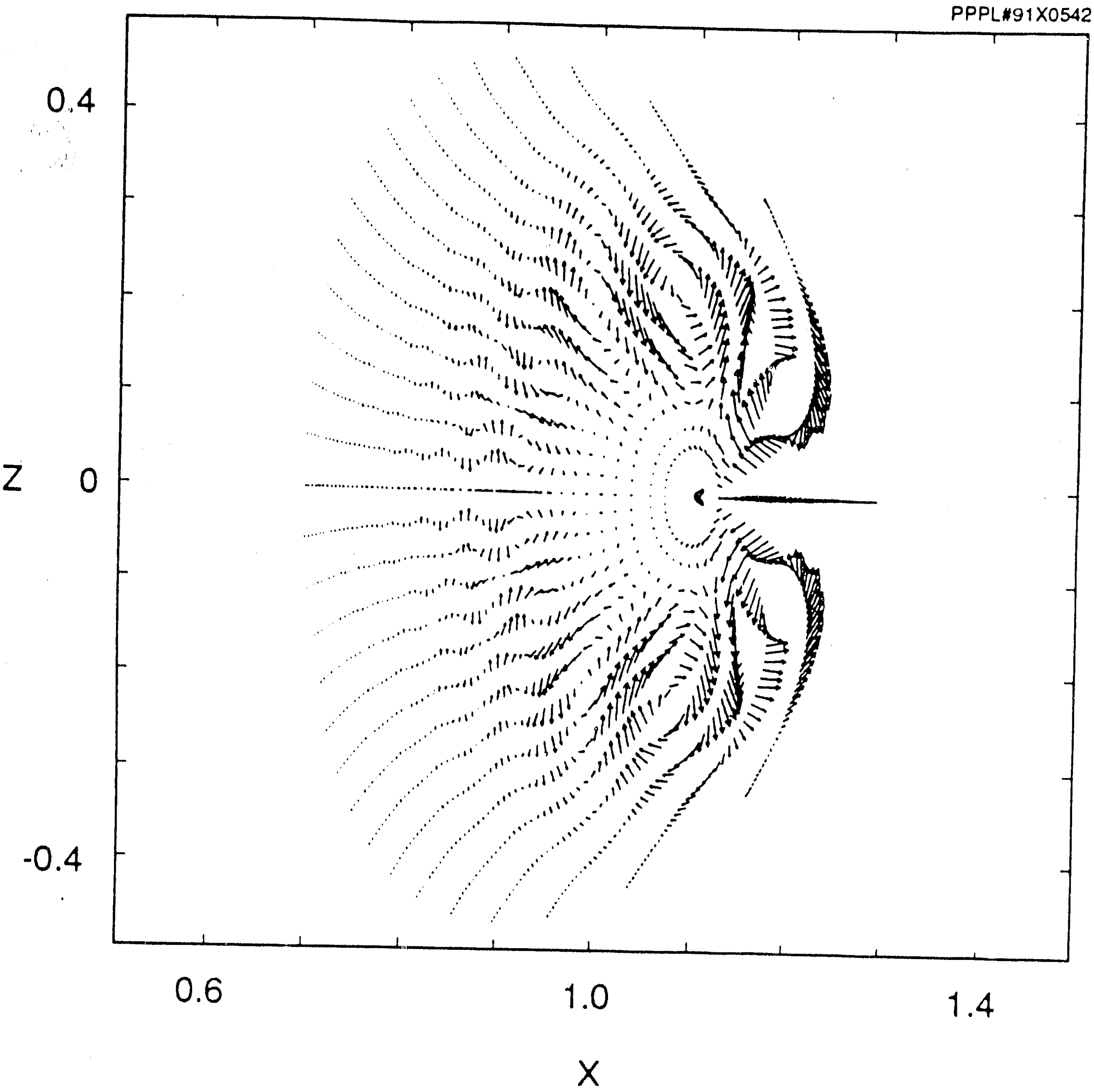

Fig. 14

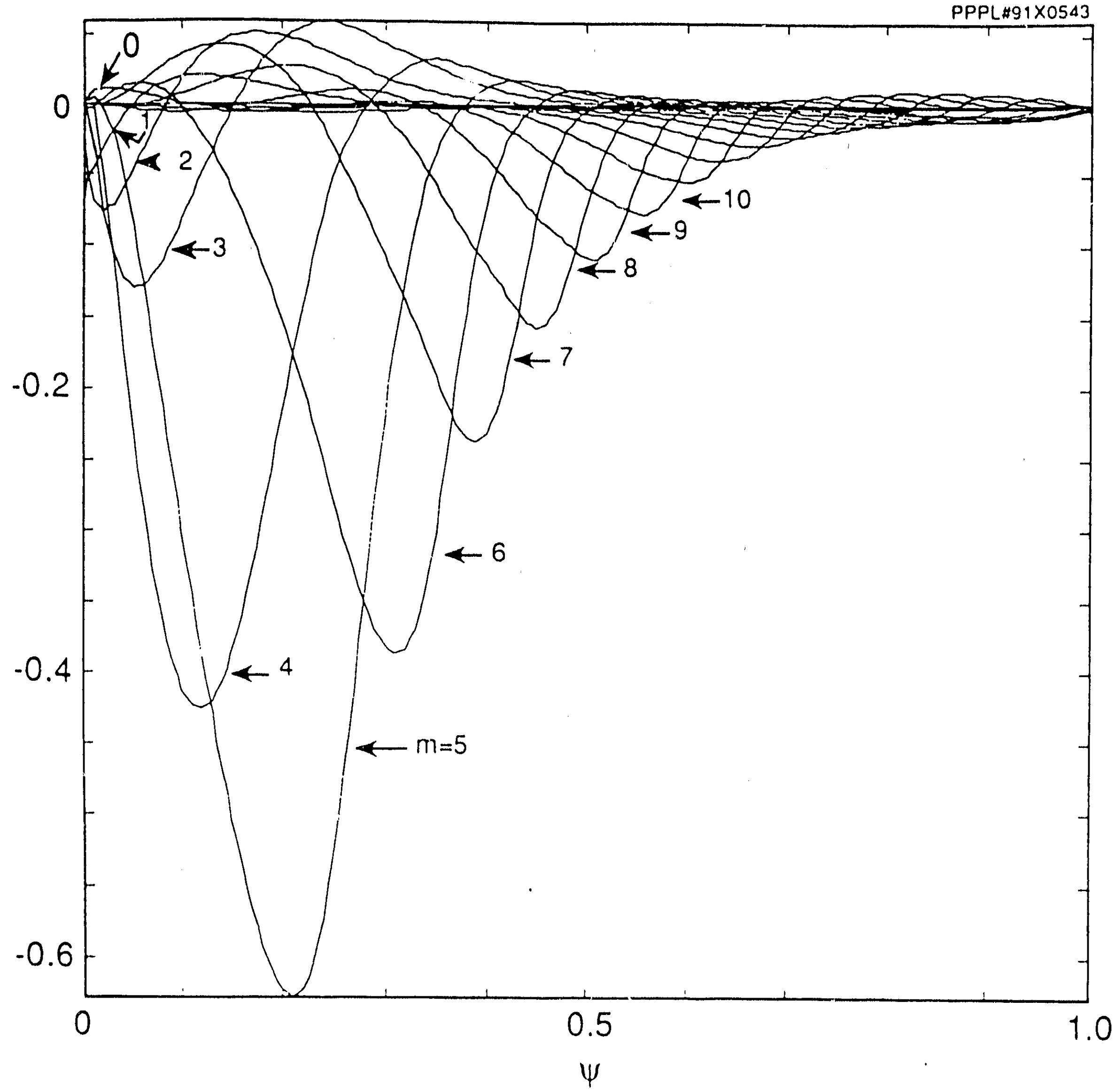

Fig. 15

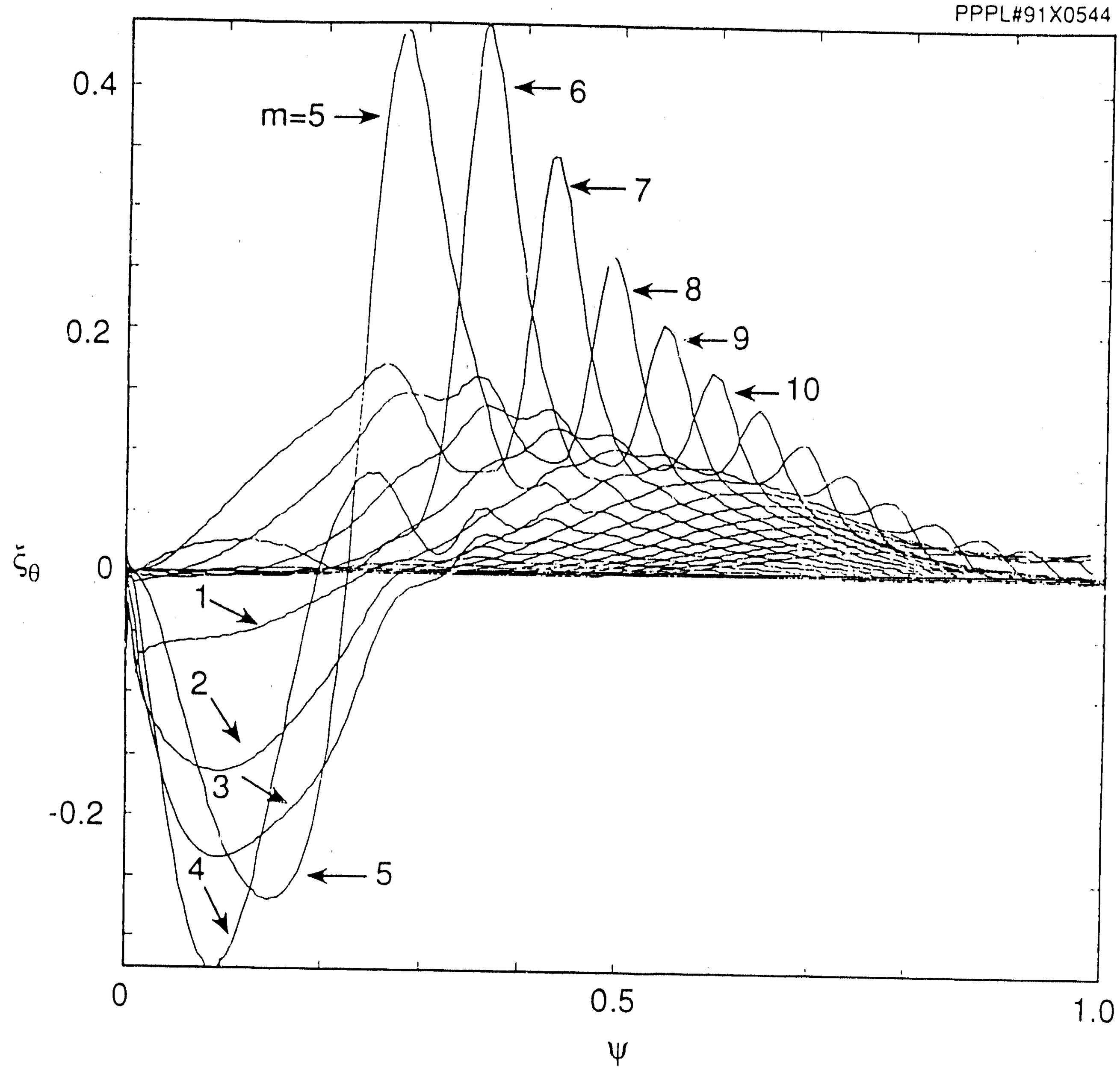

Fig. 16

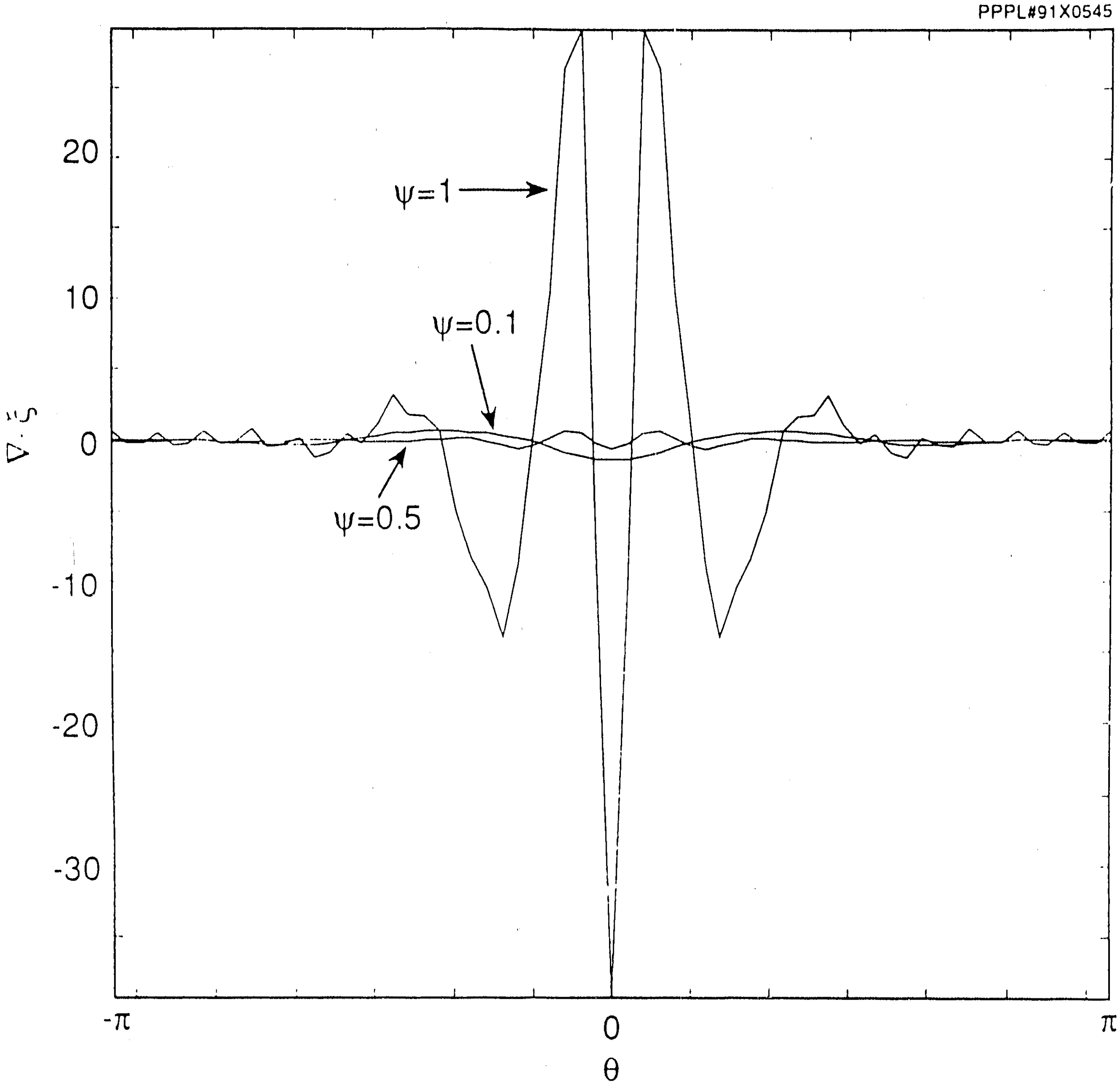

Fig. 17

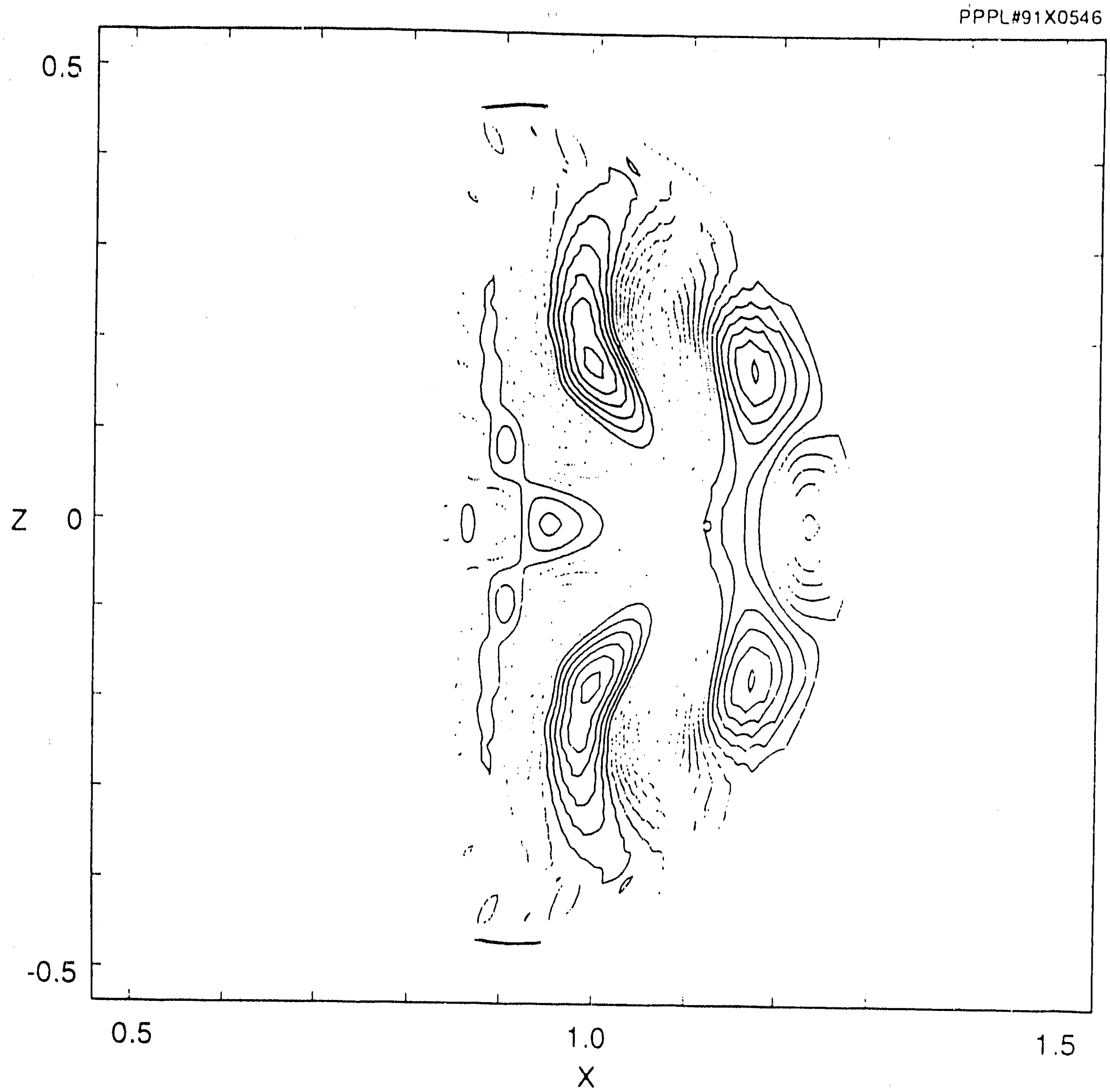

Fig. 18

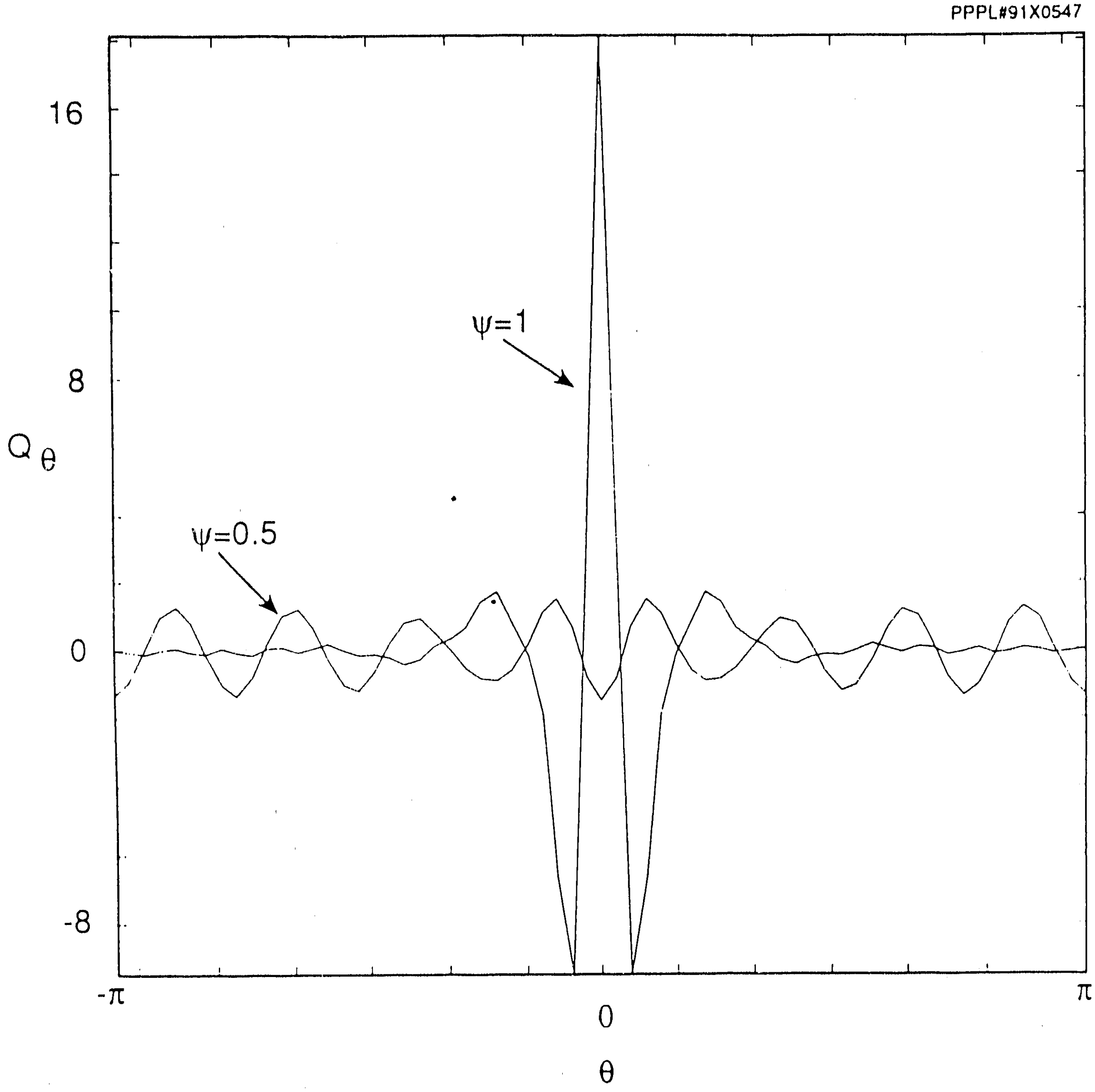

Fig. 19

PPPL #91X0548

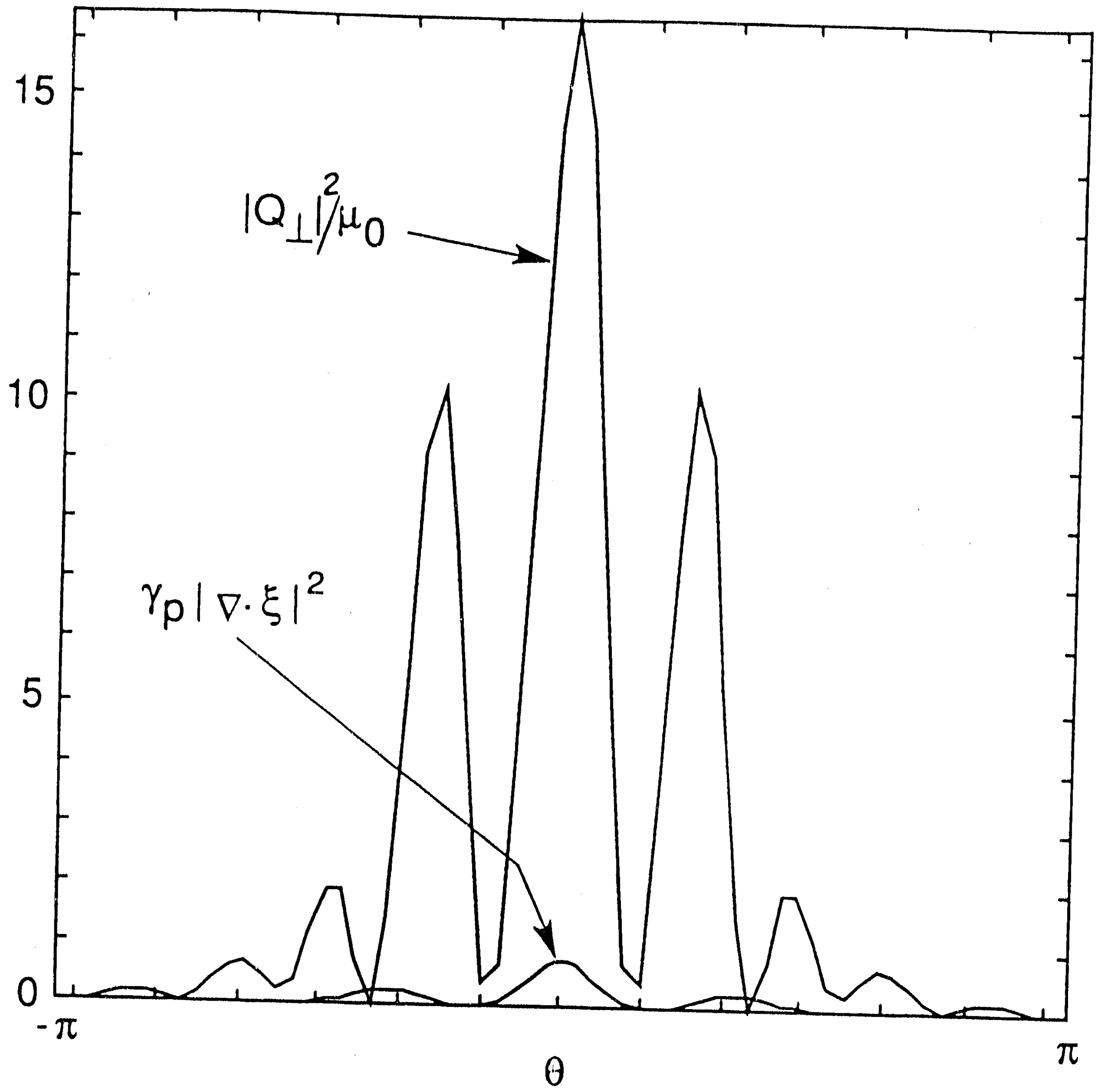

Fig. 20

EXTERNAL DISTRIBUTION IN ADDITION TO UC-420

Dr. F. Paoloni, Univ. of Wollongong, AUSTRALIA
Prof. M.H. Brennan, Univ. of Sydney, AUSTRALIA
Plasma Research Lab., Australian Nat. Univ., AUSTRALIA
Prof. I.R. Jones, Flinders Univ, AUSTRALIA
Prof. F. Cap, Inst. for Theoretical Physics, AUSTRIA
Prof. M. Heindler, Institut für Theoretische Physik, AUSTRIA
Prof. M. Goossens, Astronomisch Instituut, BELGIUM
Ecole Royale Militaire, Lab. de Phy. Plasmas, BELGIUM
Commission-European, DG. XII-Fusion Prog., BELGIUM
Prof. R. Boucique, Rijksuniversiteit Gent, BELGIUM
Dr. P.H. Sakanaka, Instituto Fisica, BRAZIL
Instituto Nacional De Pesquisas Espaciais-INPE, BRAZIL
Documents Office, Atomic Energy of Canada Ltd., CANADA
Dr. M.P. Bachynski, MPB Technologies, Inc., CANADA
Dr. H.M. Skarsgard, Univ. of Saskatchewan, CANADA
Prof. J. Teichmann, Univ. of Montreal, CANADA
Prof. S.R. Sreenivasan, Univ. of Calgary, CANADA
Prof. T.W. Johnston, INRS-Energie, CANADA
Dr. R. Bolton, Centre canadien de fusion magnétique, CANADA
Dr. C.R. James,, Univ. of Alberta, CANADA
Dr. P. Lukác, Komenského Universzita, CZECHO-SLOVAKIA
The Librarian, Culham Laboratory, ENGLAND
Library, R61, Rutherford Appleton Laboratory, ENGLAND
Mrs. S.A. Hutchinson, JET Library, ENGLAND
Dr. S.C. Sharma, Univ. of South Pacific, FIJI ISLANDS
P. Mähönen, Univ. of Helsinki, FINLAND
Prof. M.N. Bussac, Ecole Polytechnique,, FRANCE
C. Mouttet, Lab. de Physique des Milieux Ionisés, FRANCE
J. Radet, CEN/CADARACHE - Bat 506, FRANCE
Prof. E. Economou, Univ. of Crete, GREECE
Ms. C. Rinni, Univ. of Ioannina, GREECE
Dr. T. Mual, Academy Bibliographic Ser., HONG KONG
Preprint Library, Hungarian Academy of Sci., HUNGARY
Dr. B. DasGupta, Saha Inst. of Nuclear Physics, INDIA
Dr. P. Kaw, Inst. for Plasma Research, INDIA
Dr. P. Rosenau, Israel Inst. of Technology, ISRAEL
Librarian, International Center for Theo Physics, ITALY
Miss C. De Palo, Associazione EURATOM-ENEA , ITALY
Dr. G. Grosso, Istituto di Fisica del Plasma, ITALY
Prof. G. Rostangni, Istituto Gas Ionizzati Del Cnr, ITALY
Dr. H. Yamato, Toshiba Res & Devel Center, JAPAN
Prof. I. Kawakami, Hiroshima Univ., JAPAN
Prof. K. Nishikawa, Hiroshima Univ., JAPAN
Director, Japan Atomic Energy Research Inst., JAPAN
Prof. S. Itoh, Kyushu Univ., JAPAN
Research Info. Ctr., National Instit. for Fusion Science, JAPAN
Prof. S. Tanaka, Kyoto Univ., JAPAN
Library, Kyoto Univ., JAPAN
Prof. N. Inoue, Univ. of Tokyo, JAPAN
Secretary, Plasma Section, Electrotechnical Lab., JAPAN
S. Mori, Technical Advisor, JAERI, JAPAN
Dr. O. Mitarai, Kumamoto Inst. of Technology, JAPAN
J. Hyeon-Sook, Korea Atomic Energy Research Inst., KOREA
D.I. Choi, The Korea Adv. Inst. of Sci. & Tech., KOREA
Prof. B.S. Liley, Univ. of Waikato, NEW ZEALAND
Inst of Physics, Chinese Acad Sci PEOPLE'S REP. OF CHINA
Library, Inst. of Plasma Physics, PEOPLE'S REP. OF CHINA
Tsinghua Univ. Library, PEOPLE'S REPUBLIC OF CHINA
Z. Li, S.W. Inst Physics, PEOPLE'S REPUBLIC OF CHINA
Prof. J.A.C. Cabral, Instituto Superior Tecnico, PORTUGAL
Dr. O. Petrus, AL I CUZA Univ., ROMANIA
Dr. J. de Villiers, Fusion Studies, AEC, S. AFRICA
Prof. M.A. Hellberg, Univ. of Natal, S. AFRICA
Prof. D.E. Kim, Pohang Inst. of Sci. & Tech., SO. KOREA
Prof. C.I.E.M.A.T, Fusion Division Library, SPAIN
Dr. L. Stenflo, Univ. of UMEA, SWEDEN
Library, Royal Inst. of Technology, SWEDEN
Prof. H. Wilhelmson, Chalmers Univ. of Tech., SWEDEN
Centre Phys. Des Plasmas, Ecole Polytech, SWITZERLAND
Bibliotheek, Inst. Voor Plasma-Fysica, THE NETHERLANDS
Asst. Prof. Dr. S. Cakir, Middle East Tech. Univ., TURKEY
Dr. V.A. Glukhikh,Sci. Res. Inst. Electrophys.I Apparatus, USSR
Dr. D.D. Ryutov, Siberian Branch of Academy of Sci., USSR
Dr. G.A. Eliseev, I.V. Kurchatov Inst., USSR
Librarian, The Ukr.SSR Academy of Sciences, USSR
Dr. L.M. Kovrizhnykh, Inst. of General Physics, USSR
Kernforschungsanlage GmbH, Zentralbibliothek, W. GERMANY
Bibliothek, Inst. Für Plasmaforschung, W. GERMANY
Prof. K. Schindler, Ruhr-Universität Bochum, W. GERMANY
Dr. F. Wagner, (ASDEX), Max-Planck-Institut, W. GERMANY
Librarian, Max-Planck-Institut, W. GERMANY
Prof. R.K. Janev, Inst. of Physics, YUGOSLAVIA

END

DATE
FILMED
3 / 3 / 92